Stabilizing Interface between Li(2)S-P(2)S(5) Glass-Ceramic Electrolyte and Ether Electrolyte by Tuning Solvation Reaction

Bo Fan, Wenzhi Li, Zhongkuan Luo, Xianghua Zhang, Hongli Ma, Ping Fan, Bai Xue

Stabilizing Interface Between Li_2S-P_2S_5 Glass-Ceramic Electrolyte and Ether Electrolyte by Tuning Solvation Reaction

Bo Fan[a,b,c], Wenzhi Li[a], Zhongkuan Luo[d], Xianghua Zhang[e], Hongli Ma[e],Ping Fan[b], Bai Xue[b*]

[a] *College of Materials Science and Engineering, Shenzhen University, 518060 Shenzhen, China*

[b] *Shenzhen Key Laboratory of Advanced Thin Films and Applications, College of Physics and Optoelectronic Engineering, Shenzhen University, 518060 Shenzhen, China*

[c] *State Key Lab of Silicon Materials, Zhejiang University, Hangzhou 310027, China*

[d] *College of Chemistry and Environmental Engineering, Shenzhen University, 518060 Shenzhen, China*

[e] *Laboratory of Glasses and Ceramics, Institute of Chemical Science, University of Rennes 1, Rennes 35042, France*

[*] Corresponding author: baixue@szu.edu.cn

Keywords: hybrid electrolytes, Li_2S-P_2S_5, sulfide solid electrolyte, lithium-sulfur batteries, interface

ABSTRACT

Using solid–liquid hybrid electrolytes is an effective strategy to overcome the large solid/solid interfacial resistance in all-solid-state batteries and the safety problems in liquid batteries. The properties of the solid/liquid electrolyte interphase layer (SLEI) are essential for the performance of solid–liquid hybrid electrolytes. In this work, the solvation reactions between Li_2S-P_2S_5 glass-ceramic solid electrolytes and ether electrolytes were studied, and their influence on the SLEI was examined. Although 1,2-dimethoxyethane (DME) reacted with the Li_2S-P_2S_5 glass-ceramic solid electrolyte to form a dense SLEI, 1,3-dioxolane (DOL) severely corroded the solid electrolyte, resulting in a loose SLEI. Consequently, a stable SLEI formed with DME. Using a combination of the Li_2S-P_2S_5 glass-ceramic solid electrolyte and the DME-based liquid electrolyte, stable lithium plating/stripping cycles over 1000 h and a hybrid Li-S battery

that retained a specific capacity of 730 mAh g^{-1} after 200 cycles were demonstrated. The knowledge of the reactions between the sulfide electrolytes and the organic liquid electrolytes is instructive for the design of stable sulfide–liquid hybrid electrolytes for advanced batteries.

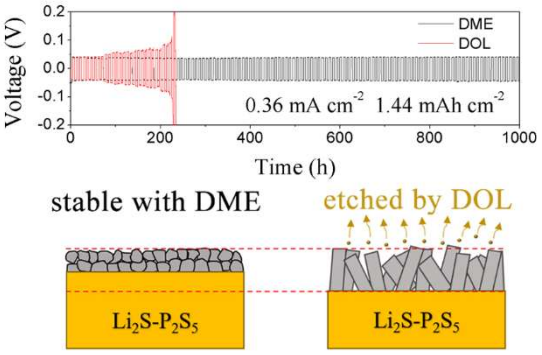

INTRODUCTION

All-solid-state batteries with high energy/power densities and enhanced safety are promising candidates for next-generation electrochemical energy storage devices.[1–4] However, they suffer from poor solid–solid contact and large interfacial resistance between the solid electrolyte and the electrode material.[5–7] Introducing a small amount of liquid electrolyte (LE) between the solid electrolyte (SE) and the electrode materials to form a so-called solid–liquid hybrid battery is an effective way to reduce the interfacial resistance.[8–11] In addition, for certain conversion-type batteries, such as Li-S batteries, a hybrid structure combining an SE membrane and a catholyte (cathode materials dissolved in LE) provides excellent rate performances owing to the enhanced liquid-phase electrochemical kinetics, showing advantages over the all-solid-state counterparts.[12] Recently, a combination of a liquid lithium solution anode and a sulfide

SE has been developed to achieve a record-high current density of 17.78 mA cm^{-2}, also demonstrating the advantages of the hybrid structure.[13]

Building stable interfaces is the key to obtaining high-performance batteries. The interfacial stability of electrolytes with a lithium metal anode[14–18] and with cathode materials[19–21] has been widely studied. For solid–liquid hybrid batteries, the properties of the solid/liquid electrolyte interphase layer (SLEI) are crucial. It has been revealed that the instability of the SLEI usually leads to a high interfacial resistance, which is detrimental for the energy densities of the batteries.[22–24] Busche et al. studied the formation process and the constitution of the SLEI when $Li_{1+x}Al_xGe_{2-x}(PO_4)_3$ (LAGP) was exposed to an ether-based LE, which contributed to the increased interfacial resistance between the SE and the LE.[22] Weiss et al. analyzed the SLEI between lithium phosphorous oxide nitride (LiPON) and various LEs by combining neutron reflectometry and a quartz crystal microbalance, and they concluded that the SLEI formed quickly when LiPON was immersed in the LE and the increasing interfacial resistance was ascribed to the filling of pinholes in the SLEI layer.[24] Until now, the studies on SLEI have not attracted sufficient attention, and mainly focused on oxide electrolytes.

Li_2S-P_2S_5 glass-ceramic SEs have excellent ionic conductivities and mechanical properties.[25] For example, $Li_7P_3S_{11}$ ($70Li_2S$-$30P_2S_5$ glass-ceramic) is a SE with an extremely high ionic conductivity of 1.7×10^{-2} S cm^{-1}.[26] β-Li_3PS_4 ($75Li_2S$-$25P_2S_5$ glass-ceramic) has a marginal ionic conductivity of 2.8×10^{-4} S cm^{-1},[27] but with better chemical stability. Ether solvents exhibit strong ability to dissolve polysulfide and good

compatibility with lithium anodes. They are widely used for Li-S batteries.[28–30] In previous work,[31-32] we observed that $75Li_2S$-$25P_2S_5$ glass-ceramics can form stable SLEIs with a conventional ether-based electrolyte, 1 M $LiN(CF_3SO_2)_2$ (LiTFSI) in 1,3-dioxolane/1,2-dimethoxyethane (DOL/DME, 50-50 vol.%), owing to the formation of a dense DME-solvated Li_3PS_4 layer at the interface. Consequently, hybrid Li-S batteries using Li_2S-P_2S_5 glass-ceramics as the separator show better cycling stability than those using certain oxide electrolyte separators.[33–34] These results encourage us to systematically explore the properties of the SLEIs between Li_2S-P_2S_5 glass-ceramic SEs and ether-based electrolytes. In this work, the solvation reactions between $75Li_2S$-$25P_2S_5$ glass-ceramic SEs and three ether-based electrolytes—DME, DOL and their mixture—were systematically studied. Based on the knowledge of the solvation reactions, a deeper understanding of the properties of the solvated interface layer was achieved. By optimizing the sulfide–liquid hybrid electrolytes, a stable lithium plating/stripping cycle over 1000 h and hybrid Li-S batteries that retained a specific capacity of 730 mAh g^{-1} after 200 cycles were demonstrated.

EXPERIMENTAL SECTION

Materials and synthesis

The chemicals used were Li_2S (99.9%, Alfa Aesar), P_2S_5 (99%, Aladdin), lithium salt LiTFSI (99%, Aladdin), 1,3-dioxolane (99.5%, Macklin), and 1,2-dimethoxyethane (99.5%, Aladdin). All the chemicals were used as is, without further purification.

Li_2S-P_2S_5 glass-ceramic electrolytes were prepared by mechanosynthesis. First, 4 g of a mixture of Li_2S and P_2S_5 with a stochiometric ratio and three tungsten carbide

grinding balls (φ = 10 mm) were put into a 45-mL tungsten carbide jar. The raw materials were ball-milled by a planetary ball-milling apparatus (Pulverisette 7, Fritsch GmbH, Germany) for 40 h. The ball-milling was conducted at 450 rpm in intermittent manner (5-min run/5-min pause) in an argon-filled glovebox (O_2 < 0.5 ppm, H_2O < 0.5 ppm). To obtain pellet samples, the resultant Li_2S-P_2S_5 glass powder was first cold-pressed into pellets with diameters of 15 mm and lengths of about 0.85 mm under a pressure of 330 MPa, after which were heat-treated under a vacuum at 260°C for 1 h.

The preparation of Li_3PS_4-coated $Li_7P_3S_{11}$ pellets followed the procedure described previously.[31] Briefly, a homogenous solution was first prepared by mixing 10 mL of a tetrahydrofuran solution containing Li_2S_6 (0.1 M) and 5 mL of an acetonitrile solution containing $Li_2S{\cdot}P_2S_5$ (0.1 M). $Li_7P_3S_{11}$ pellets were then immersed into the solution, slowly pulled up and naturally dried at room temperature in an argon-filled glovebox (O_2 < 0.5 ppm, H_2O < 0.5 ppm). The dip-coating was repeated five times. Finally, the pellets were heat-treated at 230°C under argon for 1 h. The thickness of the coating was about 500 nm.

Three ether-based LEs were prepared with different solvents, DOL, DME, and their mixture DME/DOL (50–50 vol.%). The preparation of the LEs was conducted in an argon-filled glovebox by mixing 5 mL of solvent and 1.4354 g of LiTFSI, corresponding to a molar concentration of 1 M.

Materials characterization

The phase structures of the samples were characterized by X-ray diffraction (D8 Advance, Bruker AXS GmbH, Germany). Raman spectra were recorded by a Raman

spectrometer (in Via, Renishaw Inc., UK) with a 532-nm diode-pumped solid-state laser as the excitation source. The samples for X-ray diffraction (XRD) and Raman spectroscopy were sealed with a polyimide film to protect them from air humidity. Thermal analysis was conducted using differential scanning calorimetry (DSC, DSC 3, Mettler Toledo Inc., Switzerland) and thermogravimetric analysis (TGA, TGA 55, TA Instruments Inc., DE). Both measurements used a scanning rate of 10°C min^{-1} and were conducted under N_2 flow. Inductively coupled plasma spectroscopy (ICP, Avio 200, PerkinElmer Inc., USA) was used to measure the composition of the reaction products of Li_2S-P_2S_5 and the ether solvents. The morphologies of the samples were examined by a field-emission scanning electron microscopy (SEM, SU8010, Hitachi Inc., Japan). Alternating current (AC) impedance spectroscopy was used to monitor the interfacial resistance between the Li_2S-P_2S_5 glass-ceramic pellets and the ether-based LEs. The impedance spectra were recorded by a frequency response analyzer (Solartron 1260A, Solartron Analytical Inc., UK).

Electrochemical characterization

The lithium stripping/plating was studied on symmetric cells with the structure Li/LE/SE/LE/Li. The test was conducted using a Wuhan Land CT2001 battery tester. The symmetric cells were assembled by stacking an Li foil, a Celgard2400 membrane wetted by 15 μL of an ether-based LE, an Li_3PS_4-coated $Li_7P_3S_{11}$ pellet, a Celgard2400 membrane wetted by 15 μL of an ether-based LE, and an Li foil into a coin cell. The cells were stored for 24 h before the test to complete the formation of the SLEI layer. The electrochemical impedance spectra of the cells were recorded on an

electrochemical workstation (CHI660E, CH Instruments Ins., China) with a frequency range from 0.01 to 10^5 Hz. The studied ether-based LEs included 1 M LiTFSI DME-1%$LiNO_3$, 1 M LiTFSI DME/DOL (50–50 vol.%)-1%$LiNO_3$, and 1 M LiTFSI DOL-1%$LiNO_3$.

The CR2032 coin-type hybrid lithium–sulfur batteries were assembled in an argon-filled glovebox (O_2 < 0.5 ppm, H_2O < 0.5 ppm). The structure was Li/LE/SE/LE/S-C. The cathode was made by mixing S-C composite, polyvinylidene fluoride binder, and conductive carbon black (80:10:10, wt.%) in an NMP and scraped onto Al foil, where the S-C composite was prepared by vacuum-heating the premixed sulfur and carbon (7:3) at 155°C for 12 h. After drying at 60°C for 12 h, the cathode foil was cut into Ø15-mm disks. The sulfur loading on the cathode was 0.85 mg cm^{-2}. An Li_3PS_4-coated $Li_7P_3S_{11}$ pellet was used as the SE. The LE of the anode was 15 μL of 1 M LiTFSI DME-1%$LiNO_3$. The LE of the cathode was 40 μL of 1 M LiTFSI DME-1%$LiNO_3$, 1 M LiTFSI DME/DOL (50–50 vol.%)-1%$LiNO_3$, or 1 M LiTFSI DOL-1%$LiNO_3$. The batteries were stored in a glovebox for 24 h before the test. Galvanostatic charge–discharge tests were conducted on a battery tester (CT2001, Land Ins., China) in the voltage range of 1.7–2.6 V.

RESULTS AND DISCUSSION

Solvation reactions between Li_2S-P_2S_5 and ethers

The solvation reactions between the Li_2S-P_2S_5 glass-ceramics and the ethers were studied by powder-immersion tests as follows. First, 0.6 g of powder of the 75Li_2S-25P_2S_5 glass-ceramic was immersed in 7.5 mL of DME, DOL, or DME/DOL for 48 h.

The immersion products were then characterized. Figure 1a shows the photographs of the immersion products. A color change of the supernatant was observed for all of the samples, confirming that reactions occurred during the immersion. The composition of the supernatant was quantitatively analyzed by ICP. As shown by the ICP results in Figure 1b, with a higher percentage of DOL in the solvent, more Li and P dissolved in the supernatant. These quantitative results coincide with the chromaticity of the supernatant (Figure 1a). It has been reported that $Li_2S{\cdot}P_2S_5$ can be dissolved by certain ethers and esters.[35] We therefore suspect that a similar Li_2S-P_2S_5 compound dissolved in the supernatant of the immersion products, and its solubility was higher in DOL than in DME. To prove this, 0.75 g of a mixture of Li_2S and P_2S_5 with a molar ratio of 1:1 was added into 5 mL of DOL or DME and stirred for 5 days. With the DOL, a yellow solution containing a small quantity of solid particles was obtained, while with the DME, the resulting mixture separated into a white precipitate and a yellowish supernatant (Figure S1). This further confirmed that the solubility of $Li_2S{\cdot}P_2S_5$ in the DOL was greater than that in the DME. $Li_2S{\cdot}P_2S_5$ contained dimer anion $P_2S_6^{2-}$ or chain anion $(PS_3^-)_n$.[35] The scattered negative charge distributions of these large anions weakened the ionic bonds of $Li_2S{\cdot}P_2S_5$. It is therefore expected that $Li_2S{\cdot}P_2S_5$ can be dissolved by solvents with high polarity, which would further weaken the coulombic interactions between the anions and the cations. This hypothesis was supported by the fact the acetonitrile (permittivity 35.9, donor number 14.1) had remarkably better ability to dissolve $Li_2S{\cdot}P_2S_5$ than DME (permittivity 7.2, donor number 20.0).[36] In this case, the relatively higher permittivity of DOL (7.34) than DME (7.2) [37] was assumed

be the reason for its better ability to dissolve $Li_2S{\cdot}P_2S_5$. Thus, DOL produced a severe corrosion effect on the Li_2S-P_2S_5 glass-ceramics owing to its better ability to dissolve $Li_2S{\cdot}P_2S_5$.

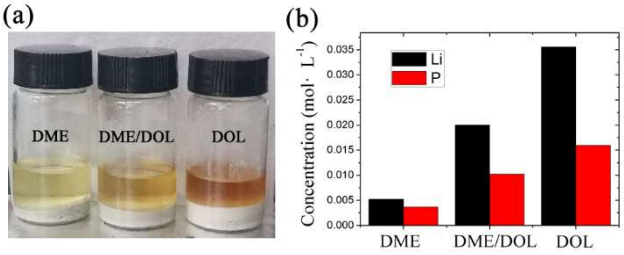

Figure 1. (a) Photographs of the $75Li_2S$-$25P_2S_5$ glass-ceramic powders after 48 h of immersion in 1,2-dimethoxyethane (DME), 1,3-dioxolane (DOL), and DME/DOL (50–50 vol.%). (b) Inductively coupled plasma (ICP) results of Li and P contents in the supernatant of the products after immersion in DOL, DME, and DME/DOL (50–50 vol.%) for 48 h.

The precipitate of the immersion test was vacuum-dried at 80°C and then analyzed by XRD (Figure 2a). The diffraction peaks different from the pristine glass-ceramic revealed the formation of solvated products. The DME-immersed sample was identified to be DME-solvated Li_3PS_4 based on previous study results.[38–39] The XRD pattern of the DOL-immersed sample has not been reported. This sample was determined to be DOL-solvated Li_3PS_4, as discussed below. Interestingly, for the sample immersed in DME/DOL, only the diffraction peaks corresponding to DME-solvated Li_3PS_4 appeared. This indicated that the solvation tendency between Li_3PS_4 and DME was stronger than that between Li_3PS_4 and DOL. In addition, the signal of the residual pristine glass-ceramic was observed (orange region). It decreased with increasing DOL content in the solvent, further confirming the strong corrosion effect of DOL on $75Li_2S$-$25P_2S_5$.

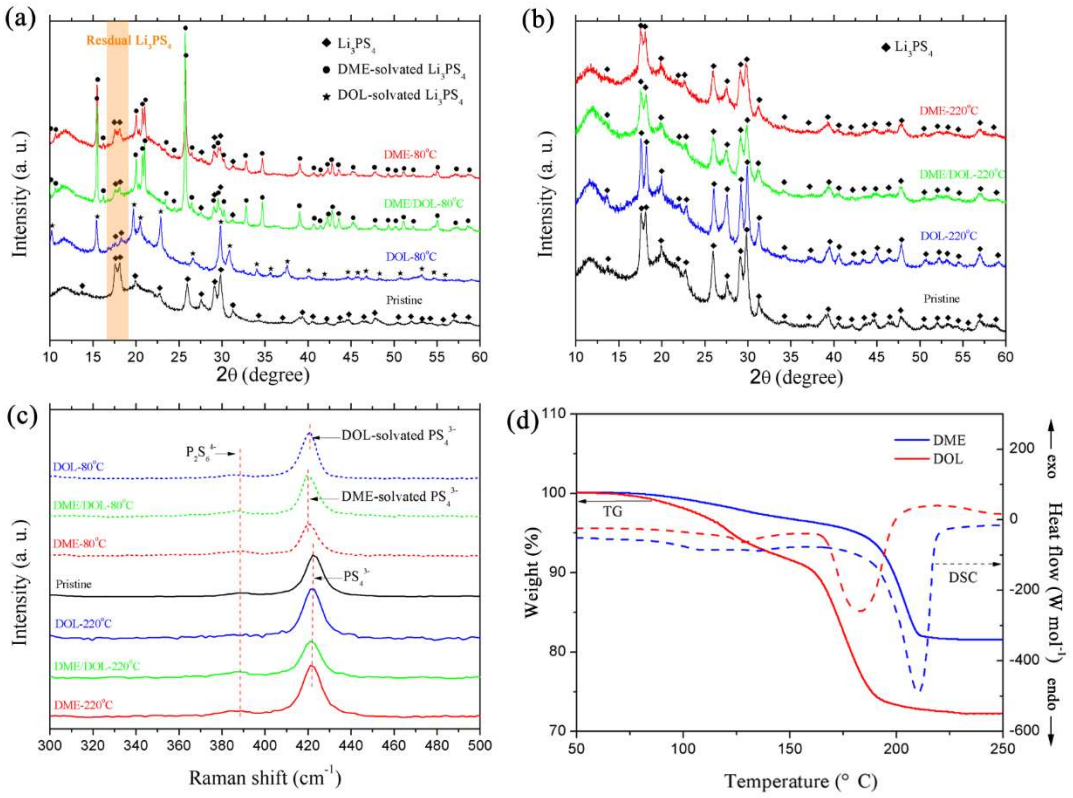

Figure 2. Characterization of the 48-h–immersed $75Li_2S$-$25P_2S_5$ powder in different solvents: (a) X-ray diffraction (XRD) pattens of the products after 80°C drying. (b) XRD patterns of the products after 220°C heat treatment. (c) Raman spectra of the pristine powder, 80°C-dried products, and 220°C-heat-treated products. (d) Differential scanning calorimetry (DSC) and thermogravimetric analysis (TGA) curves of DME-solvated Li_3PS_4 and DOL-solvated Li_3PS_4.

The precipitate of the immersion test was further heat-treated under vacuum at 220°C to completely remove the solvent. The XRD results are shown in Figure 2b. For all the studied solvents, the original β-Li_3PS_4 phase was restored. Correspondingly, the Raman peak attributed to PS_4^{3-}, which slightly shifted in the solvated Li_3PS_4 due to the solvation effect of the ether molecules, returned to 421 cm^{-1} after 220°C heat treatment. These results indicated that the solvation reactions between the $75Li_2S$-$25P_2S_5$ glass-ceramic and the studied ethers were almost reversible. This also confirmed that new

crystalline phases detected in the 80°C-dried precipitate were ether-solvated Li_3PS_4. In fact, solvated Li_3PS_4 has been widely observed in various organic solvents, which is an important intermediate during the liquid-phase synthesis of Li_2S-P_2S_5 SEs.[40–42]

Figure 2d shows the DSC and TGA results of the 80°C-dried immersion precipitate of $75Li_2S$-$25P_2S_5$. A process of weight loss was evident in the TGA curves accompanied by heat absorption, which was reflected by the endothermic peaks in the DSC curves. Both signals are associated with the desolvation of ether molecules. Based on the TGA results, the formulas of the solvated Li_3PS_4 were deduced to be Li_3PS_4·0.45DME and Li_3PS_4·0.94DOL. The solvation number of DME in the complex was only half that of DOL. This could be attributed to the fact that the two O atoms in DME could participate in the solvation process due to the flexibility of its linear backbone. In fact, the coordination of Li^+ with multiple oxygens has been widely observed for molecules with the ethylene-1,2-diether motif, such as DME, diglyme, triglyme, and poly(ethylene oxide).[43–45] Studies have illustrated that this coordination is facilitated by the torsion of the backbone to the gauche-conformation.[46] The DSC curves showed that the onset temperature of the principal desolvation process of Li_3PS_4·0.45DME was 190°C, and that of Li_3PS_4·0.94DOL was 170°C. In addition, the desolvation enthalpies normalized to the solvent molecules is 65.2 kJ mol^{-1} for DME and 35.1 kJ mol^{-1} for DOL. The higher desolvation enthalpy of DME further supported the conclusion that the solvation tendency between Li_3PS_4 and DME was stronger than that between Li_3PS_4 and DOL.

In summary, the solvation reactions between the $75Li_2S$-$25P_2S_5$ glass-ceramics and the ethers showed the following characteristics: (1) DOL showed a remarkably

better ability to dissolve $Li_2S{\cdot}P_2S_5$ than DME, and consequently, it more severely corroded the Li_2S-P_2S_5 glass-ceramics. (2) The solvation between DME and Li_3PS_4 is stronger than that between DOL and Li_3PS_4. The solvation abilities of organic solvents are generally affected by the solvent polarity, basicity, and stereochemistry. DME and DOL have similar permittivity values (7.34 for DOL and 7.2 for DME)[37] and donor numbers (18.0 for DOL and 20.0 for DME) [47], which respectively represent the polarity and the basicity. Therefore, the stereochemistry of the solvent molecules plays a key role in the solvation ability in this case. In comparison with the cyclic structure of DOL, the flexible linear backbone of DME facilitated the solvation effect of the two O atoms.

Resistance evolution of solid/liquid electrolyte interphase layer (SLEI)

The resistance evolution of the SLEI between the Li_2S-P_2S_5 glass-ceramic SE and ether-based LE was studied by an in-situ impedance spectroscopy experiment. The setup is shown in Figure 3a. Both sides of the glass-ceramic pellet were first wetted by 20 μL of LE, and were then covered by stainless-steel disks as the electrodes. The sample was finally packaged in a Swagelok mold, and the evolution of its impedance spectra was monitored by a frequency response analyzer. The impedance spectrum was composed of an incomplete semicircle at high frequency and an inclined tail at low frequency (Figure S2). The low frequency tail was attributed to polarization near the electrodes. The semicircle was due to the boundary resistance of the SE and the interfacial resistance of the SLEI.[31] The impedance spectra were fitted with the equivalent circuit shown in Figure S3. The fitting parameters are listed in Tables S1–

S3. Finally, the interfacial resistance of the SLEI was deduced from the increment of the semicircle.

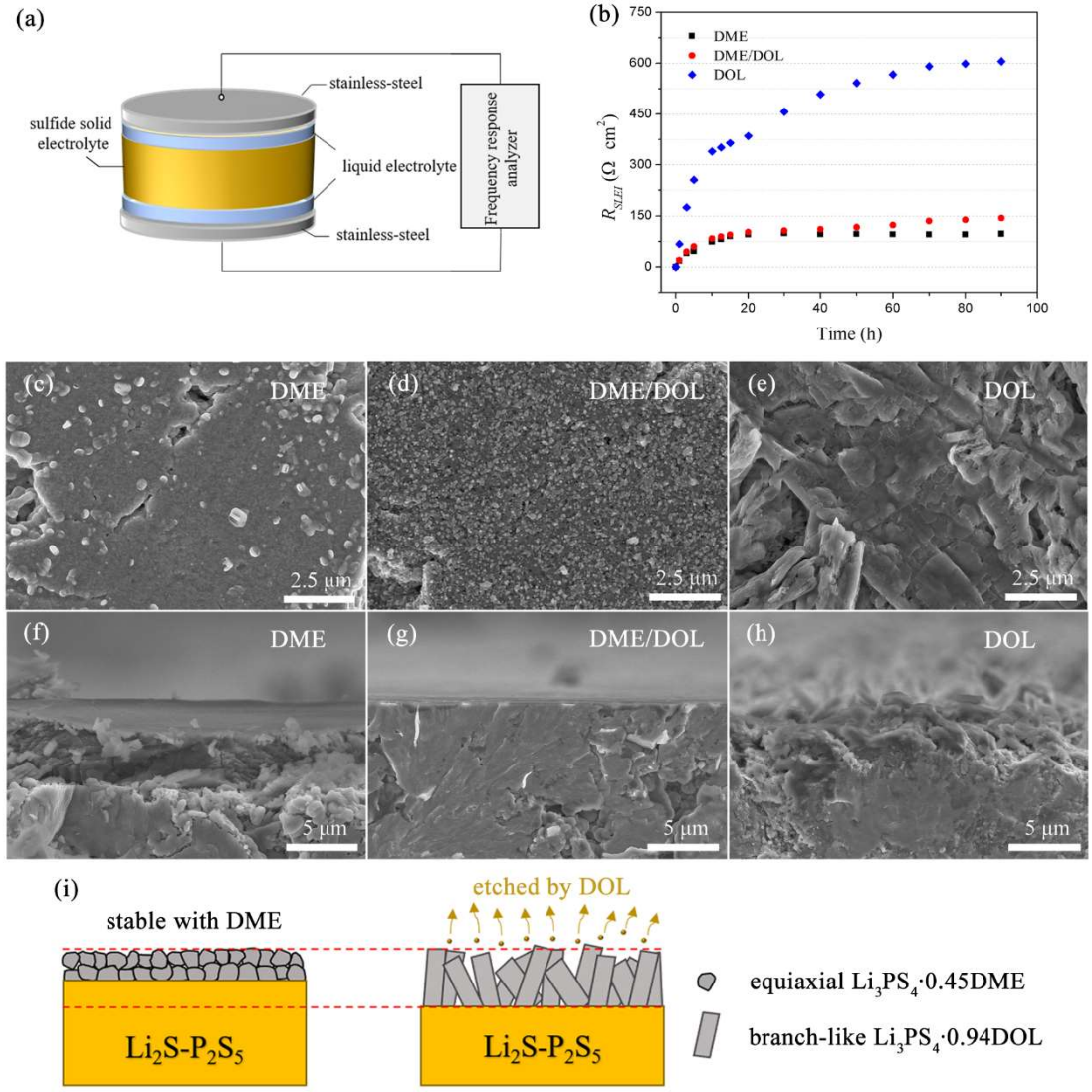

Figure 3. (a) Schematic of the setup for the interfacial resistance measurements. (b) Evolution of the interfacial resistance of $75Li_2S$-$25P_2S_5$ glass-ceramic pellets in contact with three ether-based liquid electrolytes (Les, 1 M LiTFSI in DME, DOL and DME/DOL). (c–e) Top-view and (f–h) cross-sectional scanning electron microscopy (SEM) images of $75Li_2S$-$25P_2S_5$ pellets after 90 h of contact with the ether-based LEs. (i) Influence of the solvent on solid/liquid electrolyte interphase layer (SLEI). DME and the solid electrolyte formed equiaxed crystals, and the SLEI layer was thin

and dense. DOL reacted with the solid electrolyte to form branch-like crystals, and severely etched the solid electrolyte, forming a thick and loose SLEI layer.

Figure 3b shows the evolution of the interfacial resistances between the $75Li_2S$-$25P_2S_5$ glass-ceramic pellet and the three LEs. When the DME-based LE was used, the interfacial resistance stabilized at about 95 Ω cm^2 after 15 h. When DME/DOL-based LE was used, the resistance became stable after 40 h but still slowly increased from 111 to 144 Ω cm^2 in the range of 40–90 h. When the DOL-based LE was used, the resistance increased continuously and reached 605 Ω cm^2 after 90 h. The interfacial resistance between the DME-based LE and the Li_2S-P_2S_5 glass-ceramic SE was the smallest, and it reached a stable value in the shortest time. An increase in the interfacial resistance was also observed at the oxide/liquid electrolyte interfaces,[22] which was ascribed to the gradual growth of the SLEI layers as a result of the reaction between the SE and the LE. The in-situ impedance spectroscopy experiment showed that the SLEI formed by the DME-based LE was more stable than that formed by the DOL-based LE.

The microstructures of the SE pellets after the in-situ impedance spectroscopy experiment, were characterized by top-view and cross-sectional SEM images. The pristine $75Li_2S$-$25P_2S_5$ glass-ceramic pellets showed porous surfaces owing to incomplete sintering (Figure S4). After the DME-based LE soaking, fine grains formed on the surface, which coalesced to reduce the surface roughness (Figure 3c). After the DME/DOL-based LE soaking, fine grains on the surface were also observed (Figure 3d), but less coalescence of the grains occurred and the surface was rougher than that soaked in the DME-based LE. While the DME- and DME/DOL-based LEs resulted in

very thin solvated layers (Figure 3f–g), the solvated layer formed by the DOL-based LE showed quite different features. This layer contained thick branch-like crystals stacked on the surface, and there were many pores between the crystals (Figures 3e and h). The thickness of the loose corrosion layer by the DOL-based LE was about 3 μm.

Figure 3i shows the influence of the solvent type on the SLEI layer. First, DME and DME/DOL reacted with Li_2S-P_2S_5 to form DME-solvated Li_3PS_4, while DOL reacted with Li_2S-P_2S_5 to form DOL-solvated Li_3PS_4. The different phase structures resulted in different morphologies of the solvated crystals, that is, equiaxed crystals for DME and DME/DOL and branch-like crystals for DOL. Moreover, the stronger solvation effect of DME than that of DOL reduced the surface energy of the DME-solvated Li_3PS_4, which lowered the energy barrier for nucleation. This promoted the nucleation rate of the DME-solvated Li_3PS_4 at the solid/liquid electrolyte interface, favoring the formation of fine interphase crystal grains. equiaxed and fine crystal grains were beneficial to the densification of the solvated layer. Second, the solubility of $Li_2S{\cdot}P_2S_5$ in the DOL led to severe corrosion of the Li_2S-P_2S_5 SEs. Consequently, the porosity of the solvated layers formed by the DOL and DME/DOL was larger than that by the DME. Therefore, the solvated layer of Li_2S-P_2S_5 formed by the DME-based LE was denser and thinner than the other two LEs, so that a small and stable interfacial resistance of the SLEI could be achieved.

In general, the solubility of the SE in the solvent and the crystal morphology of the solvation product were two decisive factors for the microstructure of the solvated layer formed on the surface of the Li_2S-P_2S_5 glass-ceramics. The microstructure of the

solvated layer determined the chemical stability of the SLEI between the Li_2S-P_2S_5 glass-ceramic SEs and the ether-based LEs.

Compatibility with lithium anode

To characterize the stability of the SLEI layer under the reducing environment of the lithium anode, plating/stripping cycling tests of Li/LE/SE/LE/Li symmetric cells were conducted. Here, Li_3PS_4-coated $Li_7P_3S_{11}$ pellets were used as the SE membrane. $Li_7P_3S_{11}$ has an ionic conductivity 1–2 order of magnitude higher than that of Li_3PS_4, but it would be severely decomposed by the ether solvents (Figure S5). The composite membrane possessed the high conductivity of $Li_7P_3S_{11}$ and the good stability of Li_3PS_4 in the ether solvent.

Figure 4a shows the volage profiles of the lithium plating/stripping cycling at a current density of 0.36 mA cm^{-2} and a capacity of 1.44 mAh cm^{-2}. Using the DME-based LE, the lithium symmetric cell operated stably over 1000 h, and the overpotential was only 0.040 V. When DOL/DME was used as the electrolyte solvent, the overpotential of the symmetric cell slightly increased from the initial 0.035 V to the final 0.044 V. In contrast, when using DOL as the electrolyte solvent, the overpotential began to increase at about 70 h. After 230 h, the overpotential exceeded 0.200 V, indicating that the internal resistance of the cell drastically increased. The lithium plating/stripping cycling of an Li/ SE/ Li symmetric cell was also conducted at a current density of 0.36 mA cm^{-2}. The voltage profile of this all-solid-state cell is shown in Figure S6. During a single plating/tripping process, the voltage continuously increased, which was ascribed to the void formation at the Li/SE interface.[48] In addition, the voids

caused uneven current distribution at the interface, leading to the formation of lithium dendrites. Consequently, short circuit occurred in the 5th cycle. The lithium penetration issue attracts widespread attention recently.[49] Our results demonstrated that using hybrid electrolytes alleviated the lithium penetration issue owing to the intimate contact between the lithium anode and the electrolyte.

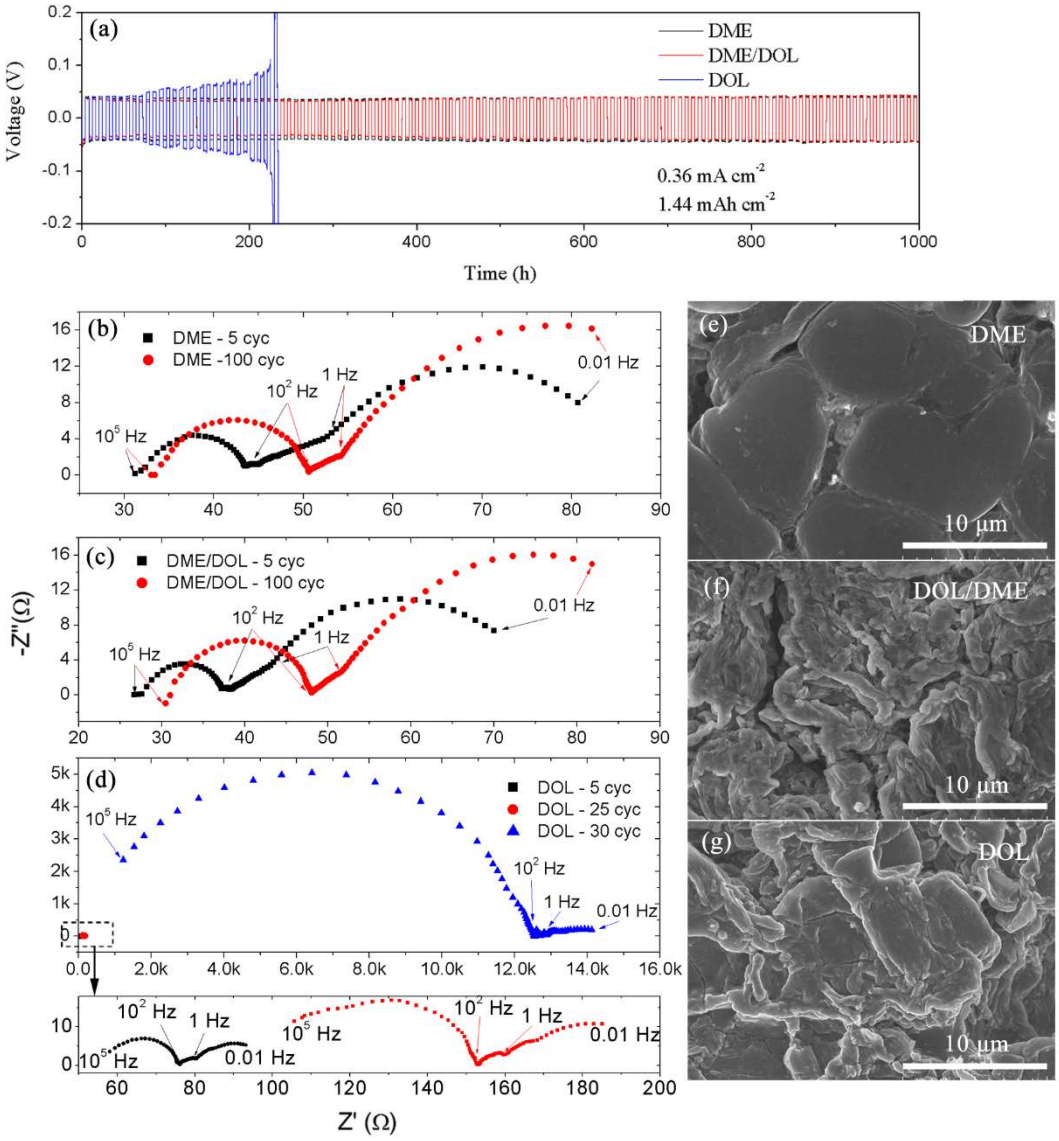

Figure 4. Lithium plating/stripping in Li/LE/ Li_2S-P_2S_5/LE/Li symmetric cells using DME, DME/DOL, and DOL as the solvents of LE. (a) Voltage profiles at 0.36 mA cm^{-2}. (b–d) Electrochemical impedance spectra of the cells after 5 and 100 cycles, respectively. SEM images

of lithium (e, f) after 125 cycles (1000 h) for the cells using DME and DME/DOL as the solvent and (g) after 30 cycles (240 h) for the cell using DOL as the solvent.

A detailed evolution of the internal resistance of the symmetric cells was studied by electrochemical impedance spectroscopy (Figures 4b–d). A high-frequency semicircle (10^5–10^2 Hz), a middle-frequency semicircle (10^2–1 Hz), and a curved low-frequency tail (< 1 Hz) were identified. Based on the frequency ranges, the high-frequency semicircle was associated with the SEI layer[50] between lithium and the LE and the SLEI layer[22] between the SE and the LE. The middle-frequency semicircle was assigned to the charge transfer of the lithium anode, which had a characteristic frequency of 1–10 Hz.[51–52] The low-frequency tail was associated with the Li-ion diffusion process around the lithium electrode. The deviation of the tail away from the ideal 45° slope was likely due to the induction behavior caused by adsorption processes,[53] although a detailed discussion of the tail is out of the scope of this work. The equivalent circuit in Figure S7 was used to fit the spectra, which quantitatively separated the internal resistance of the cells into R_e (impedance from the hybrid electrolyte), R_{int} (impedance from the SEI layer and the SLEI layer), and R_{ct} (charge transfer resistance).[54] The fitting results were listed in Table S4. When DME and DME/DOL are used as electrolyte solvents, R_e was almost unchanged and remained at about 30 Ω. R_{int} slightly increased from 9–11 Ω to 17 Ω, indicating that the SLEI was stable under the reducing environment over 1000 h. When DOL was used as the electrolyte solvent, the internal resistance of the symmetric cell increased drastically after 30 cycles (Figure 4d). R_{int}, which increased from 18 Ω to 12213 Ω, was dominating

the increase in the internal resistance. This may have been caused by two factors. First, the continuous corrosion of lithium thiophosphate by the DOL led to an enlarged resistance of the SLEI layer. Second, the $Li_2S{\cdot}P_2S_5$ dissolved in the DOL reacted with the lithium anode to form a resistive SEI layer.[55] In addition to R_{int}, R_e increased significantly after 30 cycles. A reasonable explanation for this was that the continuous reaction between the DOL and the SE membrane overconsumed the solvent, leading to poor ion conduction of the LE.

The morphology of the lithium anode was studied by SEM after the plating/stripping cycles (Figures 4e–g). No lithium dendrites were observed. Remarkably, the lithium anode of the cell using the DME-based LE showed a smooth surface after 1000 h of cycling, in sharp contrast with the branch-like lithium surfaces of the cells using the two other LEs. This demonstrated that once a stable interface between the sulfide electrolyte and the DME-based LE was established, the hybrid electrolyte was beneficial for the homogeneous plating/stripping of lithium. This could be associated with the reduced concentration polarization owing to the enhanced effective transfer number of lithium in the hybrid electrolyte.[56]

Performance of hybrid Li-S batteries

Hybrid Li-S batteries were assembled using the Li_3PS_4 coated $Li_7P_3S_{11}$ pellets as the membrane and wetting the electrodes with the ether-based LEs. The DME-based LE was chosen to wet the interface between the sulfide electrolyte membrane and the lithium anode, because it was demonstrated to show excellent stability in the previous section. The S-C cathode was wetted by different LEs. Figures 5a–c show the charge–

discharge profiles of the batteries at 0.2C (i = 0.36 mA cm^{-2}). After 200 cycles, the hybrid battery using the DME-based LE could still operate with stable charge and discharge plateaus. The second discharge plateau slightly decreased from 2.06 to 2.04 V, which benefitted from the stable SLEI layer between the Li_3PS_4 and DME-based LE. The hybrid battery using the DME/DOL-based LE showed a slightly larger internal resistance after 200 cycles, whose second discharge plateau was 2.00 V. In contrast, the battery using the DOL-based LE could not cycle stably. The overpotential increased rapidly and the battery failed in 50 cycles.

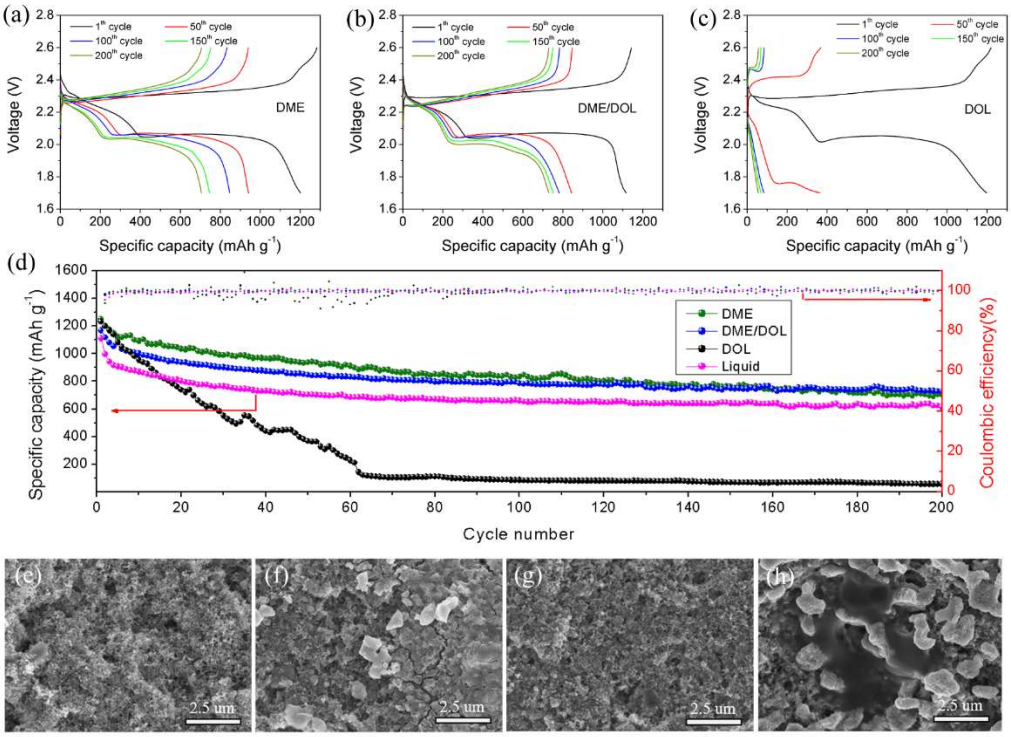

Figure 5. Performance of hybrid Li-S batteries using different LE solvents. (a–c) charge–discharge profiles of the hybrid Li-S batteries at a 0.2C rate using DME, DME/DOL, and DOL as the LE solvents, respectively. (d) Cycling performances and coulombic efficiencies of the hybrid Li-S batteries compared with those of a liquid Li-S battery. SEM images of the S-C cathode (e)

before cycling and (f–h) after 200 cycles in batteries using DME, DME/DOL, and DOL as the LE solvents, respectively.

As shown in Figure 5d, after 200 cycles at 0.2C, the coulombic efficiency of the batteries stabilized at 99.6%. The hybrid battery using the DME-based LE had a specific capacity of 706 mAh g^{-1} after 200 cycles, with a capacity retention rate of 56.4%. The hybrid battery using the DME/DOL-based LE had a specific capacity of 729 mAh g^{-1} after 200 cycles, with a capacity retention rate of 62.5%. For comparison, a liquid Li-S battery using the same batch of S-C cathodes was fabricated and its cycling performance is also shown in Figure 5d. The specific capacity of the liquid battery was 612 mAh g^{-1} after 200 cycles. Its capacity retention rate was 55.0%. The two hybrid batteries showed a higher specific capacity and better capacity retention than the liquid battery. This was attributed to the fact that the polysulfide shuttling was inhibited by the sulfide electrolyte membrane. While the hybrid electrolyte with stable SLEI layer improved the performance of the Li-S batteries by inhibiting the polysulfide shuttling effect, the unstable combination of lithium thiophosphate and the DOL-based LE degraded the battery performance. This battery continuously lost its capacity and completely failed after 60 cycles.

The SEM images of the S-C cathode after 200 cycles (Figures 5f–h) were instructive to determine the reason for the significant differences in battery performance caused by the three electrolyte solvents. The cycled cathode of the battery using the DME/DOL-based LE (Figure 5g) showed a similar porous structure as that of the pristine cathode (Figure 5e), corresponding to its good capacity retention. In contrast,

the cycled cathode of the battery using the DOL-based LE was covered by a continuous thin film, which was sensitive to an electron beam under SEM observation. Elemental analysis showed that the thin film was rich in P (Table S5). As mentioned above, severe corrosion of the Li_3PS_4 by the DOL was accompanied by the dissolution of $Li_2S{\cdot}P_2S_5$ in the LE. $Li_2S{\cdot}P_2S_5$ diffused to the cathode and formed a thin film, which passivated the reaction sites on the cathode. In addition, the thick SLEI layer between the Li_3PS_4 and the DOL significantly increased the interfacial resistance. Both factors led to the failure of the hybrid battery using the DOL-based LE.

Many typical oxide electrolytes, such as LAGP,[33] LLZO,[34] and LATP,[57] have been used to fabricate hybrid Li-S batteries. However, owing to the poor stability of the SLEI layer, these batteries always loose a large part of their capacity in the first 50 cycles (Table 1). Measures such as applying a polymer coating on the SEs can ameliorate the interfacial problem, but this introduces additional resistance and increases the overpotential of the battery. [58] Our work demonstrated that a stable SLEI layer was formed by a suitable solvation reaction between the solid and liquid electrolytes, and hybrid Li-S batteries capable of stably operating over 200 cycles can be prepared. Here, we emphasize that the low solubility of SE in the solvent and the strong solvation effect, which favored the formation of fine interphase grains, were essential for forming a dense and stable SLEI layer in the lithium thiophosphate-ether hybrid electrolyte system.

Table 1. Performance of hybrid Li-S batteries

Hybrid electrolyte	**Capacity (mAh g^{-1})**			**Second discharge plateau (V)**	**Reference**
	1st	50th	200th		
Li_3PS_4 + DME -based LE	1251	936	706	2.04	This work
Li_3PS_4 + DME/DOL-based LE	1166	846	729	2.00	This work
LAGP + DME/DOL-based LE	1386	720	--	2.08	33
LLZO + DME/DOL-based LE	1154	604	--	1.96	34
LATP + DME/DOL-based LE	978	720	--	2.01	57
Polymer-coated LATP + DME/DOL-based LE	969	890	803[a]	1.86	58

[a] Specific capacity at 150th cycle.

CONCLUSIONS

The stability of the interfaces between $75Li_2S$-$25P_2S_5$ glass-ceramic SEs and ether-based LEs was studied. It was found that the DME-based liquid electrolyte could form a stable SLEI with Li_2S-P_2S_5 glass-ceramic SEs. The Li_3PS_4 solvation effect of DME was stronger than that of DOL. This favored the formation of fine crystal grains of the solvated Li_3PS_4, which constituted a dense solvated layer at the solid/liquid electrolyte interface. Meanwhile, the corrosion effect of DME on the Li_2S-P_2S_5 glass ceramic SEs was weaker than that of DOL. Both factors were important for the formation of a stable and compact DME-solvated Li_3PS_4 layer at the interface, which was necessary obtain a stable solid/liquid electrolyte interface. Benefitting from this stable solid/liquid electrolyte interface, stable lithium plating/stripping cycles over 1000 h and hybrid Li-S batteries that retained specific capacities of 730 mAh g^{-1} after 200 cycles were demonstrated. This work deepens the understanding of SLEI layers by examining the solvation reactions between the sulfide electrolytes and the ether-based LEs. The results are instructive for designing stable sulfide–liquid hybrid electrolytes

for advanced batteries.

ASSOCIATED CONTENT

Supporting Information. The support information is available free of charge.

Notes. The authors declare no competing financial interest.

ACKNOWLEDGEMENT

The work is financially supported by National Natural Science Foundation of China (NFSC) project (No. 51702216), Natural Science Foundation of Guangdong Province (No. 2021A1515011725), Stable Support Plan for Shenzhen Higher Education Institutions (No. 20200811211215001), Shenzhen Science and Technology Foundation (JCYJ20210324095808023), and State Key Laboratory of Silicon Materials Visiting Scholar Fund (SKL2020-10).

REFERENCES

1. Kato, Y.; Hori, S.; Saito, T.; Suzuki, K.; Hirayama, M.; Mitsui, A.; Yonemura, M.; Iba, H.; Kanno, R., High-Power All-Solid-State Batteries Using Sulfide Superionic Conductors. *Nat. Energy* **2016,** *1*, 16030.

2. Jiang, M.; Liu, G.; Zhang, Q.; Zhou, D.; Yao, X., Ultrasmall Li_2S-Carbon Nanotube Nanocomposites for High-Rate All-Solid-State Lithium–Sulfur Batteries. *ACS Appl. Mater. Interfaces* **2021,** *13*, 18666-18672.

3. Zhang, Q.; Cai, L.; Liu, G.; Li, Q.; Jiang, M.; Yao, X., Selenium-Infused Ordered Mesoporous Carbon for Room-Temperature All-Solid-State Lithium–Selenium Batteries with Ultrastable Cyclability. *ACS Appl. Mater. Interfaces* **2020,** *12*, 16541-16547.

4. Zhang, Z.; Wu, L.; Zhou, D.; Weng, W.; Yao, X., Flexible Sulfide Electrolyte Thin Membrane with Ultrahigh Ionic Conductivity for All-Solid-State Lithium Batteries. *Nano Lett.* **2021,** *21*, 5233-5239.

5. Judez, X.; Zhang, H.; Li, C.; Eshetu, G. G.; González-Marcos, J. A.; Armand, M.; Rodriguez-Martinez, L. M., Review—Solid Electrolytes for Safe and High Energy Density Lithium-Sulfur Batteries: Promises and Challenges. *J. Electrochem. Soc.* **2017,** *165*, A6008-A6016.

6. Gao, Z.; Sun, H.; Fu, L.; Ye, F.; Zhang, Y.; Luo, W.; Huang, Y., All-Solid-State Batteries: Promises,

Challenges, and Recent Progress of Inorganic Solid-State Electrolytes for All-Solid-State Lithium Batteries. *Adv. Mater.* **2018,** *30*, 1870122.

7. Wang, Y.; Sahadeo, E.; Rubloff, G.; Lin, C.-F.; Lee, S. B., High-Capacity Lithium Sulfur Battery and Beyond: A Review of Metal Anode Protection Layers and Perspective of Solid-State Electrolytes. *J. Mater. Sci.* **2018,** *54*, 3671-3693.

8. Zhao, C.-Z.; Zhao, B.-C.; Yan, C.; Zhang, X.-Q.; Huang, J.-Q.; Mo, Y.; Xu, X.; Li, H.; Zhang, Q., Liquid Phase Therapy to Solid Electrolyte–Electrode Interface in Solid-State Li Metal Batteries: A Review. *Energy Storage Mater.* **2020,** *24*, 75-84.

9. Zhang, Z. Y.; Jin, C. H.; Liang, X. L.; Chen, Q.; Peng, L.-M., Current-Voltage Characteristics and Parameter Retrieval of Semiconducting Nanowires. *Appl. Phys. Lett.* **2006,** *88*, 073102.

10. Xu, B.; Duan, H.; Liu, H.; Wang, C. A.; Zhong, S., Stabilization of Garnet/Liquid Electrolyte Interface Using Superbase Additives for Hybrid Li Batteries. *ACS Appl. Mater. Interfaces* **2017,** *9*, 21077-21082.

11. Wang, C.; Sun, Q.; Liu, Y.; Zhao, Y.; Li, X.; Lin, X.; Banis, M. N.; Li, M.; Li, W.; Adair, K. R.; Wang, D.; Liang, J.; Li, R.; Zhang, L.; Yang, R.; Lu, S.; Sun, X., Boosting the Performance of Lithium Batteries with Solid-Liquid Hybrid Electrolytes: Interfacial Properties and Effects of Liquid Electrolytes. *Nano Energy* **2018,** *48*, 35-43.

12. Yu, X.; Bi, Z.; Zhao, F.; Manthiram, A., Hybrid Lithium–Sulfur Batteries with a Solid Electrolyte Membrane and Lithium Polysulfide Catholyte. *ACS Appl. Mater. Interfaces* **2015,** *7*, 16625-16631.

13. Peng, J.; Wu, D.; Song, F.; Wang, S.; Niu, Q.; Xu, J.; Lu, P.; Li, H.; Chen, L.; Wu, F., High Current Density and Long Cycle Life Enabled by Sulfide Solid Electrolyte and Dendrite-Free Liquid Lithium Anode. *Adv. Funct. Mater.* **2021**, 2105776.

14. Liu, W.; Liu, P.; Mitlin, D., Review of Emerging Concepts in Sei Analysis and Artificial Sei Membranes for Lithium, Sodium, and Potassium Metal Battery Anodes. *Adv. Energy Mater.* **2020,** *10*, 2002297.

15. Chen, H.; Pei, A.; Lin, D.; Xie, J.; Yang, A.; Xu, J.; Lin, K.; Wang, J.; Wang, H.; Shi, F.; Boyle, D.; Cui, Y., Uniform High Ionic Conducting Lithium Sulfide Protection Layer for Stable Lithium Metal Anode. *Adv. Energy Mater.* **2019,** *9*, 1900858.

16. Wu, F.; Chu, F.; Ferrero, G. A.; Sevilla, M.; Fuertes, A. B.; Borodin, O.; Yu, Y.; Yushin, G., Boosting High-Performance in Lithium–Sulfur Batteries Via Dilute Electrolyte. *Nano Lett.* **2020**, 5391–5399.

17. Zhao, Y.; Ye, Y.; Wu, F.; Li, Y.; Li, L.; Chen, R., Anode Interface Engineering and Architecture Design for High-Performance Lithium-Sulfur Batteries. *Adv. Mater.* **2019,** *31*, e1806532.

18. Wan, H.; Liu, S.; Deng, T.; Xu, J.; Zhang, J.; He, X.; Ji, X.; Yao, X.; Wang, C., Bifunctional Interphase-Enabled $Li_{10}GeP_2S_{12}$ Electrolytes for Lithium–Sulfur Battery. *ACS Energy Lett.* **2021,** *6*, 862-868.

19. Edström, K.; Gustafsson, T.; Thomas, J. O., The Cathode–Electrolyte Interface in the Li-Ion Battery. *Electrochimica Acta* **2004,** *50*, 397-403.

20. Duan, H.; Yin, Y.-X.; Shi, Y.; Wang, P.-F.; Zhang, X.-D.; Yang, C.-P.; Shi, J.-L.; Wen, R.; Guo, Y.-G.; Wan, L.-J., Dendrite-Free Li-Metal Battery Enabled by a Thin Asymmetric Solid Electrolyte with Engineered Layers. *J. Am. Chem. Soc.* **2018,** *140*, 82-85.

21. Yuan, W.; Qiu, Z.; Wang, C.; Yuan, Y.; Yang, Y.; Zhang, X.; Ye, Y.; Tang, Y., Design and Interface Optimization of a Sandwich-Structured Cathode for Lithium-Sulfur Batteries. *Chem. Eng. J.* **2020,** *381*.

22. Busche, M. R.; Drossel, T.; Leichtweiss, T.; Weber, D. A.; Falk, M.; Schneider, M.; Reich, M. L.; Sommer, H.; Adelhelm, P.; Janek, J., Dynamic Formation of a Solid-Liquid Electrolyte Interphase and

Its Consequences for Hybrid-Battery Concepts. *Nat. Chem.* **2016,** *8*, 426-434.

23. Oh, D. Y.; Nam, Y. J.; Park, K. H.; Jung, S. H.; Cho, S.-J.; Kim, Y. K.; Lee, Y.-G.; Lee, S.-Y.; Jung, Y. S., Excellent Compatibility of Solvate Ionic Liquids with Sulfide Solid Electrolytes: Toward Favorable Ionic Contacts in Bulk-Type All-Solid-State Lithium-Ion Batteries. *Adv. Energy Mater.* **2015,** *5*, 1500865.

24. Weiss, M.; Seidlhofer, B.-K.; Geiß, M.; Geis, C.; Busche, M. R.; Becker, M.; Vargas-Barbosa, N. M.; Silvi, L.; Zeier, W. G.; Schröder, D.; Janek, J., Unraveling the Formation Mechanism of Solid–Liquid Electrolyte Interphases on Lipon Thin Films. *ACS Appl. Mater. Interfaces* **2019,** *11*, 9539-9547.

25. Murayama, M.; Sonoyama, N.; Yamada, A.; Kanno, R., Material Design of New Lithium Ionic Conductor, Thio-LISICON, in the Li_2S–P_2S_5 System. *Solid State Ionics* **2004,** *170*, 173-180.

26. Seino, Y.; Ota, T.; Takada, K.; Hayashi, A.; Tatsumisago, M., A Sulphide Lithium Super Ion Conductor Is Superior to Liquid Ion Conductors for Use in Rechargeable Batteries. *Energy Environ. Sci.* **2014,** *7*, 627-631.

27. Hayashi, A.; Hama, S.; Minami, T.; Tatsumisago, M., Formation of Superionic Crystals from Mechanically Milled Li_2S–P_2S_5 Glasses. *Electrochem. Commun.* **2003,** *5*, 111-114.

28. Meisner, Q. J.; Rojas, T.; Dietz Rago, N. L.; Cao, J.; Bareño, J.; Glossmann, T.; Hintennach, A.; Redfern, P. C.; Pahls, D.; Zhang, L.; Bloom, I. D.; Ngo, A. T.; Curtiss, L. A.; Zhang, Z., Lithium–Sulfur Battery with Partially Fluorinated Ether Electrolytes: Interplay between Capacity, Coulombic Efficiency and Li Anode Protection. *J. Power Sources* **2019,** *438*, 226939.

29. Wang, L.; Ye, Y.; Chen, N.; Huang, Y.; Li, L.; Wu, F.; Chen, R., Development and Challenges of Functional Electrolytes for High-Performance Lithium–Sulfur Batteries. *Adv. Funct. Mater.* **2018,** *28*, 1800919.

30. Zheng, J.; Ji, G.; Fan, X.; Chen, J.; Li, Q.; Wang, H.; Yang, Y.; DeMella, K. C.; Raghavan, S. R.; Wang, C., High-Fluorinated Electrolytes for Li–S Batteries. *Adv. Energy Mater.* **2019,** *9*, 1803774.

31. Fan, B.; Xu, Y.; Ma, R.; Luo, Z.; Wang, F.; Zhang, X.; Ma, H.; Fan, P.; Xue, B.; Han, W., Will Sulfide Electrolytes Be Suitable Candidates for Constructing a Stable Solid/Liquid Electrolyte Interface? *ACS Appl. Mater. Interfaces* **2020,** *12*, 52845-52856.

32. Xu, Y.-H.; Li, W.-Z.; Fan, B.; Fan, P.; Luo, Z.-K.; Wang, F.; Zhang, X.-H.; Ma, H.-L.; Xue, B., Stabilizing Electrode/Electrolyte Interface in Li-S Batteries Using Liquid/Solid Li_2S-P_2S_5 Hybrid Electrolyte. *Appl. Surf. Sci.* **2021,** *546*, 149034.

33. Wang, Q.; Jin, J.; Wu, X.; Ma, G.; Yang, J.; Wen, Z., A Shuttle Effect Free Lithium Sulfur Battery Based on a Hybrid Electrolyte. *Phys. Chem. Chem. Phys.* **2014,** *16*, 21225-21229.

34. Naguib, M.; Sharafi, A.; Self, E. C.; Meyer, H. M.; Sakamoto, J.; Nanda, J., Interfacial Reactions and Performance of $Li_7La_3Zr_2O_{12}$-Stabilized Li–Sulfur Hybrid Cell. *ACS Appl. Mater. Interfaces* **2019,** *11*, 42042-42048.

35. Delnick, F. M.; Yang, G.; Self, E. C.; Meyer, H. M.; Nanda, J., Investigation of Complex Intermediates in Solvent-Mediated Synthesis of Thiophosphate Solid-State Electrolytes. *J. Phys. Chem. C* **2020,** *124*, 27396-27402.

36. Fan, B.; Zhang, Q.; Luo, Z.; Zhang, X.; Ma, H.; Fan, P.; Xue, B., Influence of Precipitate/Supernatant Ratio During Liquid-Phase Synthesis of Solid Electrolyte $Li_7P_3S_{11}$. *Solid State Ionics* **2019,** *343*, 115073.

37. Herr, T.; Fischer, P.; Tübke, J.; Pinkwart, K.; Elsner, P., Increasing the Energy Density of the Non-Aqueous Vanadium Redox Flow Battery with the Acetonitrile-1,3-Dioxolane–Dimethyl Sulfoxide Solvent Mixture. *J. Power Sources* **2014,** *265*, 317-324.

38. Xue, B.; Fan, B.; Li, B.; Chen, L.; Wang, F.; Luo, Z. K.; Zhang, X. H.; Ma, H. L., Solvent-Assisted

Ball Milling for Synthesizing Solid Electrolyte $Li_7P_3S_{11}$. *J. Am. Ceram. Soc.* **2019,** *102*, 3402-3410.

39. Ito, S.; Nakakita, M.; Aihara, Y.; Uehara, T.; Machida, N., A Synthesis of Crystalline $Li_7P_3S_{11}$ Solid Electrolyte from 1,2-Dimethoxyethane Solvent. *J. Power Sources* **2014,** *271*, 342-345.

40. Wang, Z. X.; Jiang, Y.; Wu, J.; Jiang, Y.; Huang, S. S.; Zhao, B.; Chen, Z. W.; Zhang, J. J., Reaction Mechanism of Li_2S-P_2S_5 System in Acetonitrile Based on Wet Chemical Synthesis of $Li_7P_3S_{11}$ Solid Electrolyte. *Chem. Eng. J.* **2020,** *393*.

41. Wang, H.; Hood, Z. D.; Xia, Y.; Liang, C., Fabrication of Ultrathin Solid Electrolyte Membranes of β-Li_3PS_4 Nanoflakes by Evaporation-Induced Self-Assembly for All-Solid-State Batteries. *J. Mater. Chem. A* **2016,** *4*, 8091-8096.

42. Liu, Z.; Fu, W.; Payzant, E. A.; Yu, X.; Wu, Z.; Dudney, N. J.; Kiggans, J.; Hong, K.; Rondinone, A. J.; Liang, C., Anomalous High Ionic Conductivity of Nanoporous β-Li_3PS_4. *J. Am. Chem. Soc.* **2013,** *135*, 975-978.

43. Zhang, C.; Yamazaki, A.; Murai, J.; Park, J.-W.; Mandai, T.; Ueno, K.; Dokko, K.; Watanabe, M., Chelate Effects in Glyme/Lithium Bis(Trifluoromethanesulfonyl)Amide Solvate Ionic Liquids, Part 2: Importance of Solvate-Structure Stability for Electrolytes of Lithium Batteries. *J. Phys. Chem. C* **2014,** *118*, 17362-17373.

44. Liu, N.; Li, H.; Jiang, J.; Huang, X.; Chen, L., Li−Biphenyl−1,2-Dimethoxyethane Solution: Calculation and Its Application. *J. Phys. Chem. B* **2006,** *110*, 10341-10347.

45. Sutjianto, A.; Curtiss, L. A., Li^+-Diglyme Complexes: Barriers to Lithium Cation Migration. *J. Phys. Chem. A* **1998,** *102*, 968-974.

46. Ferreira, B. A.; Müller-Plathe, F.; Bernardes, A. T.; De Almeida, W. B., A Comparison of Li^+ Transport in Dimethoxyethane, Poly(Ethylene Oxide) and Poly(Tetramethylene Oxide) by Molecular Dynamics Simulations. *Solid State Ionics* **2002,** *147*, 361-366.

47. Yao, Y.-X.; Chen, X.; Yan, C.; Zhang, X.-Q.; Cai, W.-L.; Huang, J.-Q.; Zhang, Q., Regulating Interfacial Chemistry in Lithium-Ion Batteries by a Weakly Solvating Electrolyte. *Angew. Chem. Int. Ed.* **2021,** *60*, 4090-4097.

48. Kasemchainan, J.; Zekoll, S.; Spencer Jolly, D.; Ning, Z.; Hartley, G. O.; Marrow, J.; Bruce, P. G., Critical Stripping Current Leads to Dendrite Formation on Plating in Lithium Anode Solid Electrolyte Cells. *Nat. Mater.* **2019,** *18*, 1105-1111.

49. Liu, G.; Weng, W.; Zhang, Z.; Wu, L.; Yang, J.; Yao, X., Densified Li_6PS_5Cl Nanorods with High Ionic Conductivity and Improved Critical Current Density for All-Solid-State Lithium Batteries. *Nano Lett.* **2020,** *20*, 6660-6665.

50. Wu, B.; Lochala, J.; Taverne, T.; Xiao, J., The Interplay between Solid Electrolyte Interface (SEI) and Dendritic Lithium Growth. *Nano Energy* **2017,** *40*, 34-41.

51. Xu, K., Nonaqueous Liquid Electrolytes for Lithium-Based Rechargeable Batteries. *Chem. Rev.* **2004,** *104*, 4303-4418.

52. Zhang, W.; Richter, F. H.; Culver, S. P.; Leichtweiss, T.; Lozano, J. G.; Dietrich, C.; Bruce, P. G.; Zeier, W. G.; Janek, J., Degradation Mechanisms at the $Li_{10}GeP_2S_{12}$/$LiCoO_2$ Cathode Interface in an All-Solid-State Lithium-Ion Battery. *ACS Appl. Mater. Interfaces* **2018,** *10*, 22226-22236.

53. Orazem, M. E.; Tribollet, B., *Electrochemical Impedance Spectroscopy*. John Wiley & Sons Inc. : Hoboken, New Jersey, 2008.

54. Fu, L.; Wang, X.; Wang, L.; Wan, M.; Li, Y.; Cai, Z.; Tan, Y.; Li, G.; Zhan, R.; Seh, Z. W.; Sun, Y., A Salt-in-Metal Anode: Stabilizing the Solid Electrolyte Interphase to Enable Prolonged Battery Cycling. *Adv. Funct. Mater.* **2021,** *31*, 2010602.

55. Lin, Z.; Liu, Z.; Fu, W.; Dudney, N. J.; Liang, C., Phosphorous Pentasulfide as a Novel Additive for High-Performance Lithium-Sulfur Batteries. *Adv. Funct. Mater.* **2013,** *23*, 1064-1069.

56. Huo, H.; Chen, Y.; Luo, J.; Yang, X.; Guo, X.; Sun, X., Rational Design of Hierarchical "Ceramic-in-Polymer" and "Polymer-in-Ceramic" Electrolytes for Dendrite-Free Solid-State Batteries. *Adv. Energy Mater.* **2019,** *9*, 1804004.

57. Wang, S.; Ding, Y.; Zhou, G.; Yu, G.; Manthiram, A., Durability of the $Li_{1+x}Ti_{2-x}Al_x(PO_4)_3$ Solid Electrolyte in Lithium–Sulfur Batteries. *ACS Energy Lett.* **2016,** *1*, 1080-1085.

58. Yu, X.; Manthiram, A., Enhanced Interfacial Stability of Hybrid-Electrolyte Lithium-Sulfur Batteries with a Layer of Multifunctional Polymer with Intrinsic Nanoporosity. *Adv. Funct. Mater.* **2019,** *29*, 1805996.